Genesis of the coupling of internal wave modes in the Strait of Messina

Gaëlle Casagrande [a,*], Alex Warn Varnas [b], Yann Stéphan [a], Thomas Folégot [c]

[a] *Service Hydrographique et Océanographique de la Marine, 13 rue Le Chatellier, 29200 Brest, France*
[b] *Naval Research Laboratory, Stennis Space Centre, MS 39529, USA*
[c] *NATO Undersea Research Centre, Viale San Bartolomeo 400, 19126 La Spezia, Italy*

ARTICLE INFO

ABSTRACT

The internal waves in the south of the Strait of Messina (Italy) are studied using observational data and numerical simulations. The observational data consisted of SAR images, XBT probes, CTD yoyos and thermistor string profiles from the Coastal Ocean Acoustic Changes at High Frequencies (COACH06) cruise. The numerical Lamb model was used to solve the fully nonlinear, nonhydrostatic Boussinesq equations on an f-plane. The model is 2.5 dimensional with spatial variation in a vertical plane extending along depth and in along-stream direction, and neglects derivatives in cross-stream direction.

Eleven out of fifteen SAR images contained internal wave events for the month of October 2006. From these images, we estimated some of the internal wave characteristics: a least square fit of the front positions of the southwards propagating internal wave trains gives a propagation speed of 1.00 m s^{-1} and a time of release of the bore of about 2 h after maximum northwards tidal flow at Punta Pezzo. Nonhydrostatic dispersion leads to a wavelength increase between the first two internal solitary waves of the trains of 40 m km^{-1}.

Our *in-situ* data were used to initialize and evaluate the Lamb model. An EOF analysis was applied to the data and the model outputs. The first three empirical functions contain over 99% of the variability. The data and the model results are in very good qualitative and quantitative agreement, giving a propagation depth of the internal solitary wave train around 90 m with a pycnocline oscillating from 80 to 130 m.

Using the first two EOFs, an original method for detecting internal waves was developed by analyzing the scatter diagram of the first EOF projection coefficient versus the second EOF projection coefficient. This distribution has a specific "crescent shape" showing that the first two projection coefficients are not independent in the presence of internal wave events. The "crescent shape" signature of the internal waves can be used as an internal wave detector.

© 2009 Elsevier B.V. All rights reserved.

1. Introduction

The Strait of Messina is a rich dynamic area where many ocean features can be encountered. It separates the Italian Peninsula from the island of Sicily and is a natural connection between the Tyrrhenian Sea in the north and the Ionian Sea in the south (Fig. 1). The strait is a narrow channel whose smallest cross-sectional area is 0.3 km^2 in the sill region. The sill raises to within 80 m of the surface at the shallowest point. The water depth increases gently in the northern part of the strait whereas the slope is steeper in the south basin (15 km away from the sill, the depth is 400 m in the north basin, and 800 m in the south). Throughout the year, two water masses are encountered in the strait: the Tyrrhenian surface water and the colder and saltier Levantine Intermediate Water from the Ionian Sea.

Although the Strait of Messina has been known since ancient times as an area of strong currents and vortices (represented by the two mythological monsters Scylla and Charybdis in Homer Odyssey, 800 B.C.), more than 2000 years elapsed before modern scientific oceanographic measurements were carried out in this area. The French vice-consul Ribaud gave a fairly detailed description of the currents in the strait in 1824, but it was not until 1922–23 that an extensive oceanographic survey was made by the Italian oceanographer Vercelli (1925) with the research vessel Marsigli. The data collected are still considered to be the most detailed and systematic data from the Strait of Messina and were used and processed by Hopkins et al. in 1984. What really initialized the intense study of the Strait of Messina was the first satellite observation of internal waves made by SEASAT on 15 September 1978 (Alpers and Salusti, 1983). In the following years, oceanographic campaigns were carried out to measure internal solitary waves north and south of the strait. In the following years, a considerable number of scientific studies of internal solitary waves in the Strait of Messina were made through *in-situ* and satellite observations (Alpers and Salusti, 1983; Hopkins et al., 1984; Griffa et al., 1986; Marullo and Santoleri, 1986; Sapia and Salusti, 1987; Gerkema, 1994; Brandt et al., 1997; Brandt et al., 1998).

From the measurements carried out, a current distribution has emerged. The dominating role of semidiurnal tides was described in

* Corresponding author. Tel.: +33 2 98 37 77 59; fax: +33 2 98 22 18 64.
E-mail addresses: gaelle.casagrande@shom.fr (G. Casagrande),
varnas@nrlssc.navy.mil (A. Warn Varnas), yann.stephan@shom.fr (Y. Stéphan),
folegot@nurc.nato.int (T. Folégot).

1. REPORT DATE **15 NOV 2008**	2. REPORT TYPE	3. DATES COVERED **00-00-2008 to 00-00-2008**
4. TITLE AND SUBTITLE **Genesis of the coupling of internal wave modes in the Strait of Messina**		5a. CONTRACT NUMBER
		5b. GRANT NUMBER
		5c. PROGRAM ELEMENT NUMBER
6. AUTHOR(S)		5d. PROJECT NUMBER
		5e. TASK NUMBER
		5f. WORK UNIT NUMBER
7. PERFORMING ORGANIZATION NAME(S) AND ADDRESS(ES) **Naval Research Laboratory,Stennis Space Center,MS,93943**		8. PERFORMING ORGANIZATION REPORT NUMBER
9. SPONSORING/MONITORING AGENCY NAME(S) AND ADDRESS(ES)		10. SPONSOR/MONITOR'S ACRONYM(S)
		11. SPONSOR/MONITOR'S REPORT NUMBER(S)
12. DISTRIBUTION/AVAILABILITY STATEMENT **Approved for public release; distribution unlimited**		
13. SUPPLEMENTARY NOTES		
14. ABSTRACT **see report**		
15. SUBJECT TERMS		

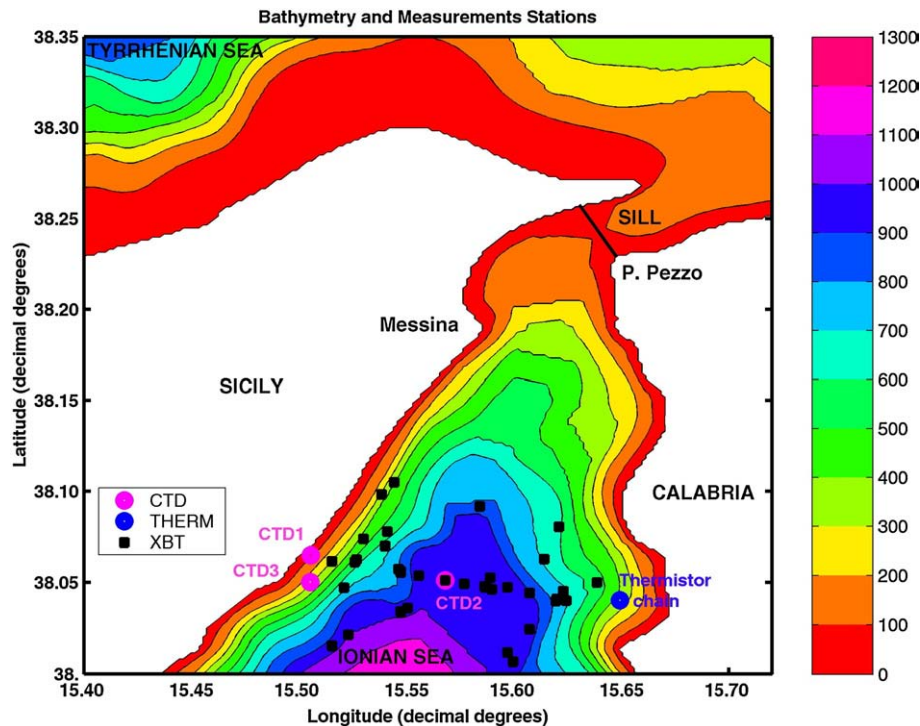| 16. SECURITY CLASSIFICATION OF:			17. LIMITATION OF ABSTRACT **Same as Report (SAR)**	18. NUMBER OF PAGES **14**	19a. NAME OF RESPONSIBLE PERSON
a. REPORT **unclassified**	b. ABSTRACT **unclassified**	c. THIS PAGE **unclassified**			

Fig. 1. Bathymetry of the Strait of Messina. The points show the measurement positions: blue dot is the thermistor string position, pink dots indicate the CTD stations, and black dots represent XBT probes.

detail, and the influence of baroclinicity on the formation of the velocity field in the strait was qualitatively determined in Hopkins et al. (1984) and Mosetti (1988). At the sill, a stationary surface current is flowing in the southwards direction (≈ 0.10 m s^{-1} time-averaged velocity) and a bottom current is flowing in the opposite direction towards the Tyrrhenian Sea (≈ 0.13 m s^{-1} time-averaged velocity). The Ionian water coming from the south is saltier and heavier, the relative density difference is of the order of 0.001. Superimposed on these stationary currents are the tidal currents originating from the co-oscillation of the water masses of the strait with the tides of the adjacent seas. During maximum tidal flow from the Tyrrhenian Sea to the Ionian Sea (rema scendente) and inversely (rema montante), only one type of water is encountered over the sill, thus annihilating the two-layer structure over the sill: the tidal barotropic aspect of water motion was analyzed by Defant (1961). The time-averaged interface between these two water masses is at a depth of 150 m in the adjacent basins but at 30 m around and above the strait which means an uplift of 120 m from the adjoining basins (Bignami and Salusti, 1990). Although tidal sea surface displacements are very small in the strait of Messina (the order of 10 cm), Defant (1940) explained the existence of strong currents in the strait by the fact that the tides for the open strait boundaries oscillate almost in opposition, thus leading to a sea surface slope of 1–2 cm km^{-1} generating strong currents (Mosetti, 1988) as high as 3 m s^{-1} in the sill region during spring tides (Bignami and Salusti, 1990).

The strong barotropic tidal flow over a steep bathymetry in a stably stratified environment represents the ideal recipe for internal wave generation (Zeilon, 1912). Baines (1973, 1982) has demonstrated the generation process analytically. Hydrodynamic modelling shows that tidal flow over steep topography creates an interfacial depression of the pycnocline and generates an internal bore (Del Ricco, 1982; Lamb, 1994; Mosetti, 1988; Brandt et al., 1997; Warn Varnas et al., 2003, 2005, 2007). In the Strait of Messina, during rema montante when the heavier Levantine Intermediate Water crosses the sill, the pycnocline moves upwards at the sill and is depressed in the northern basin. The depression generates a southwards and a northwards propagating

bore. The northwards propagating bore steepens and disintegrates into solitary waves whereas the southwards propagating bore is stopped by the sill. When the semidiurnal tide reverses to rema scendente, the southwards propagating internal depression undergoes a hydraulic jump over the sill and into the southern basin where it propagates away from the sill. As it propagates, nonlinear effects steepen its leading edge until it disintegrates into a series or "train" of interfacial nonlinear short internal waves. This disintegration is due to effects of frequency and amplitude dispersions, as well described in Warn Varnas et al. (2007). Internal waves in the Strait of Messina are characterized by a propagation speed between 0.80 to 1.00 m s^{-1}, with oscillations of temperature up to 2 °C amplitude. When the train is well formed, 4 to 10 internal solitary waves per train can be observed with periods ranging from 8 to 30 min, covering an average total duration of about 2 h (Alpers and Salusti, 1983).

In this paper, we present an original way of characterizing the internal waves in the Strait of Messina by using their multimodal structure. For October 2006, fifteen SAR images gave the internal waves characteristics which are used to tune a Lamb numerical model for the Strait of Messina. The model was initialized from *in-situ* data and numerical outputs are compared with the COACH06 cruise oceanographic measurements (late October–beginning of November 2006) by applying an Empirical Orthogonal Function (EOF) analysis. Using the crescent-shape scatter plot formed by the first and second EOF projection coefficients, it was possible to characterize the presence of internal waves south of the Strait. Section 2 describes the dataset and the EOF analysis of the *in-situ* data. Section 3 presents the model and Section 4 discusses the scatter diagram results. Section 5 contains a summary and conclusions.

2. Dataset exploitation

The dataset consisted of SAR images (October 2006) and *in-situ* hydrographical data (4–11 November 2006) such as XBT probes, CTD yoyos and a thermistor chain.
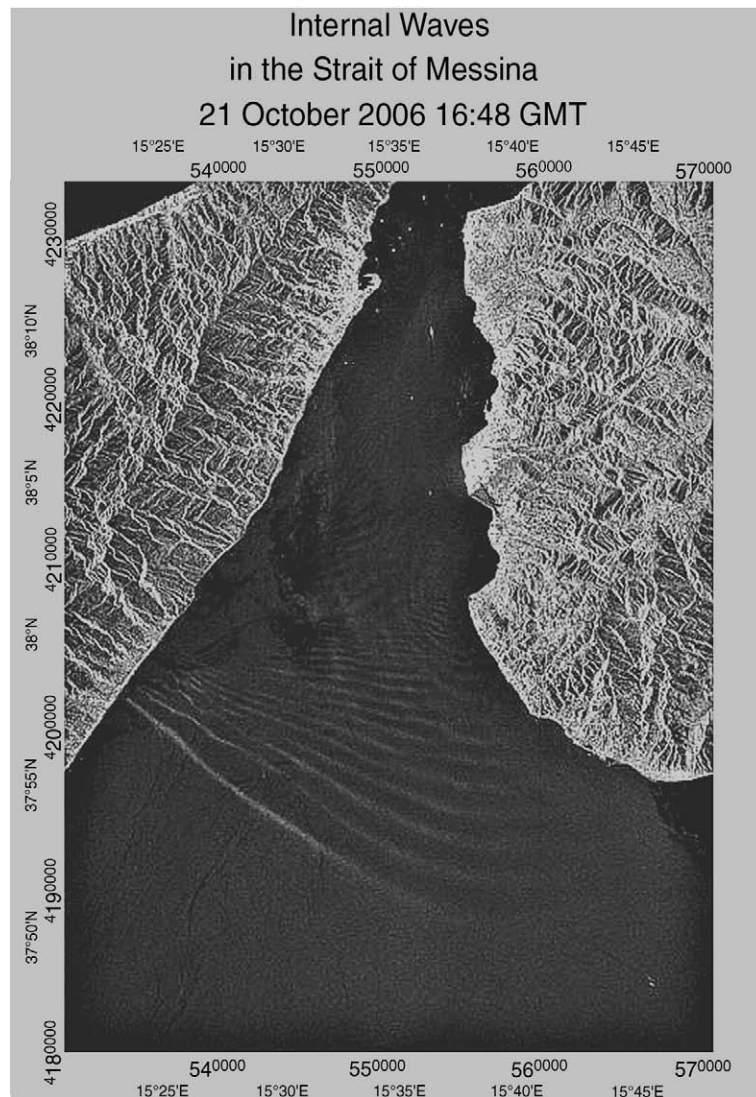
Fig. 2. SAR image from RADARSAT1 satellite with a clear internal solitary waves train signature seen on 21 October 2006, 16:48 UTC.

2.1. SAR images

The propagating solitary waves are seen as isopycnal depressions (Osborne and Burch, 1980). When such interfacial depressions propagate, they generate a downstream flow convergence that increases the surface roughness and upstream flow divergence that tends to smooth the surface roughness. SAR are most sensible to such surface roughness and are able to picture internal waves as trains of bright (convergence) and dark (divergence) streaks (Alpers and Salusti, 1983; Apel and Jackson, 2004). The first time that tidal bores have been identified on a SAR image in the Strait of Messina was on 15 September 1978 (Alpers and Salusti, 1983). Since then, the SAR data have been widely used in internal wave studies in the Strait of Messina (Alpers et al., 1996; Brandt et al., 1997). Global Ocean Associates (GOA), founded by Dr. John R. Apel in 1996 and funded by the Office of Naval Research, made a worldwide Atlas of Internal Solitary-like Waves (GOA, 2004) using SAR images. In this Atlas, internal solitary wave characteristics were computed for the Strait of Messina and the adjacent sea areas, by using SAR images from ERS-1/2 satellites for a period ranging from beginning of 1991 to December 1995. On the whole period, 77 manifestations of internal waves could be delineated out of 160 overflights. That study showed that sea surface manifestations of internal solitary wave trains are observed more frequently

during summer when a strong seasonal pycnocline is known to be present. Furthermore, sea surface manifestations of southwards propagating internal solitary wave trains are more frequent than northwards propagating ones. For the month of October, on average,

Table 1
SAR image characteristics.

Date	Time (UTC)	Δt (IM/MNF)	d.Sill (m)	n	Length (m)	d.1/2 (m)
3rd Oct 2006	9:02	08:17	22703	5	3784	946
5th Oct 2006	5:01	15:25	46637	7	6168	1852
6th Oct 2006	9:08	18:08	59757	5	6000	2571
8th Oct 2006	21:01	17:06	54769	12	17700	2187
11th Oct 2006	16:43	10:54	31634	2	1500	1416
15th Oct 2006	20:41	09:52	29142	3	3429	1714
21st Oct 2006	16:48	13:58	41651	12	10769	2051
21st Oct 2006	20:52	18:02	56456	10	13021	2532
		6:00	14142	1	x	x
24th Oct 2006	17:00	12:52	35833	4	3789	1428
24th Oct 2006	20:58	16:50	51210	2	2032	2034

'Date' and 'time' of the SAR image. 'Δt (IM/MNF)' is the time difference between the SAR image and the previous occurrence of maximum northwards flow in P. Pezzo, 'd.Sill' is the distance between the observed internal wave train and the sill, 'n' is the number of solitary waves in the train, 'length' is the length of the whole train, 'd.1/2' is the spatial separation between the first and second waves.

there are 10 observations of internal solitary wave trains out of 14 overflights south of the Strait of Messina.

In our dataset, 15 SAR images for October 2006 were obtained from the ENVISAT observation satellite (launched in 2002 by the European Space Agency, ESA) and from the RADARSAT-I satellite (launched in 1995 by the Canadian Space Agency, CSA). Eleven of them presented internal solitary wave train signatures (Fig. 2). Table 1 summarizes, for each SAR image showing an internal wave event, the date and time of the image, the time difference between the SAR image and the previous occurrence of maximum northwards flow in P. Pezzo, the distance of the first internal solitary wave from the sill, the number of solitary waves in the train, the length of the whole train and the spatial separation between the first and second waves. The internal wave train propagation velocity, the time of release of the bore and the spatial separation between the first two internal waves of the trains have been computed from these data in Sections 2.1.1 and 2.1.3. These parameters give a statistical representation of the distinctive south-wards propagating internal waves formed at the sill.

2.1.1. Internal wave propagation velocity and time of release of the bore

A time versus distance diagram delineating the propagation of internal bores is shown in order to estimate the propagation velocity of the internal solitary wave train and the time of release of internal bores from the sill (Fig. 3 top). The "distance" is measured along a mean path between the sill and the centre of the wave fronts, which is inferred from the available SAR images; "time" refers to the time between the occurrence of the previous maximum northwards flow in P. Pezzo and the moment when SAR image was taken. The line is a least square fit that yields an estimated propagation speed of 1.00 m s^{-1}. The time of release of the bore at the sill is about 2 h, which is in excellent agreement with the Atlas of Internal Waves (GOA, 2004), which with the same methodology yields a propagation velocity of 0.91 m s^{-1} and a time of release of 1 to 5 h. We have described in the introduction that the bore was generated by an interfacial depression at the lee side of the sill by the northwards tidal flow, and is released into the southern basin when the tidal flow weakens and reverses southwards. The time of release of the bore is then the time between the maximum
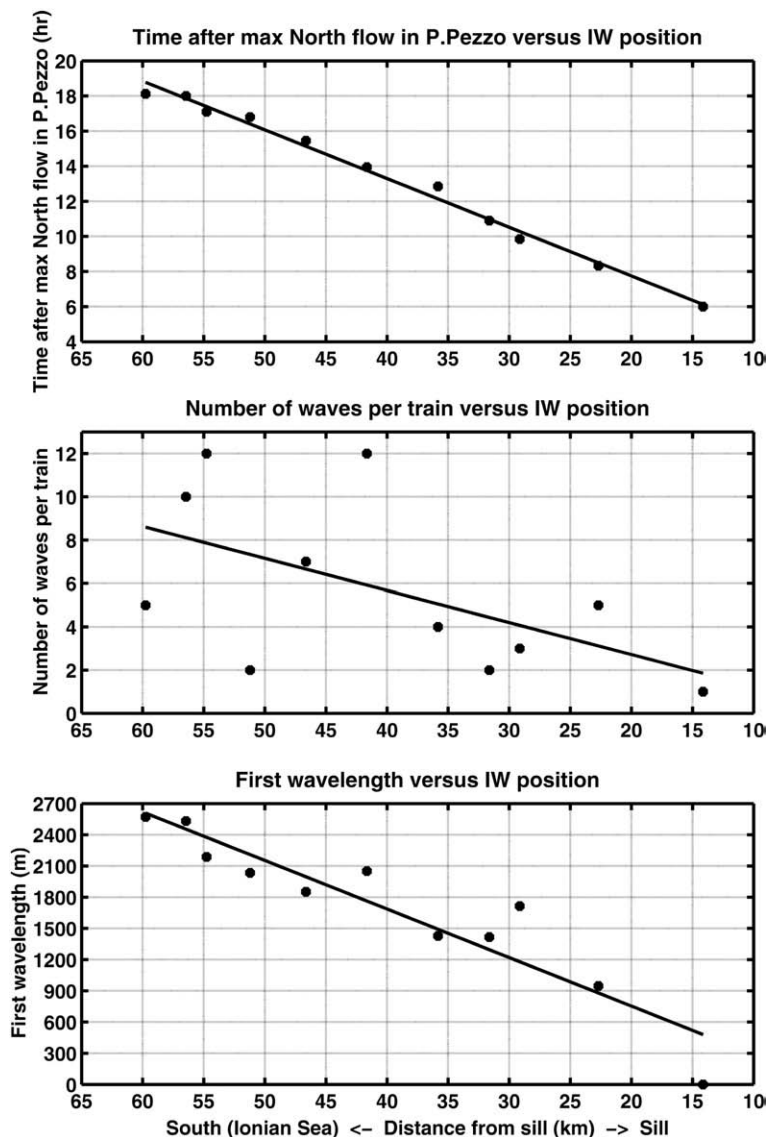

Fig. 3. Study of the 11 SAR images showing internal wave trains south of Messina Strait (Ionian Sea). Top, space–time diagram showing the propagation of the front of internal waves. Middle, number of internal solitary waves per train versus the IW train position in the south of the strait. Bottom, spatial separation between the first two internal solitary waves of each train as a function of the IW train position. "Distance from sill" (*x*-axis) is the IW train position represented as the distance between the first wave and the sill. South is considered to be on the left side, north on the right. "Time" is the temporal separation between the maximum northwards flow in Punta Pezzo and the time of the SAR image. The lines are least square fits.

northwards flow in P. Pezzo and the slack water corresponding to the tidal flow reversal when the bore undergoes its hydraulic jump over the sill. Looking at tide tables for the month of October 2006, this time of release varies from 2.5 to 4 h, fitting in the interval of 1 to 5 h mentioned in the Atlas of Internal Waves (2004).

2.1.2. Number of waves versus the distance away from the sill

The second graph of Fig. 3 (middle) illustrates the disintegration of the internal bore into a train of internal solitary waves. It represents the number of internal solitary waves per train versus the distance to the strait. Only one SAR image shows an event close to the strait, that is one observation at 14 km from the sill. This observation can be interpreted as a bore that has not yet disintegrated. It is only at least 23 km away from the sill that the number of waves increases, showing when the bore disintegrates into internal solitary waves. This means that the bore has to travel a very long distance before disintegrating into a wave train. This effect is mainly due to the strong increase in the bottom depth south of the sill of the strait as discussed in Griffa et al. (1986).

2.1.3. Spatial separation between the first two waves for a well formed internal wave train

Fig. 3 (bottom) shows the spatial separation between the first two internal waves of the propagating wave trains as a function of the distance from the sill. The first wave of the train has bigger amplitude and velocity than the second wave, meaning that the wavelength between the first two internal solitary waves increases as the train propagates. In the *Atlas of Internal Waves* (2004), the spatial separation ranges from 500 m to 1900 m. For our set of images, the wavelength ranges from 1300 m (30 km south of the sill) to 2500 m (60 km south of the sill), meaning that the spatial separation between the first two waves increases by 40 m km^{-1} as the train travels southwards. Still this figure must be considered cautiously as it is very difficult to measure exactly the spatial separation of the first two waves because of the imperfect circular shape of the wave fronts (see wave front on Fig. 2).

2.2. In-situ data

During the COACH06 cruise (4–11 November 2006), the French R/V Beautemps-Beaupré made CTD and XBT measurements. One thermistor chain was also deployed (Fig. 1).

49 XBT probes were launched between 4 and 7 November in the southern basin. These XBT measurements provided temperature profiles, and density was computed from Unesco equation of state. The density profiles show great variability, illustrating the presence of internal solitary waves (Fig. 4 top). The XBT measurements were used to check whether the distance from the coasts would influence the
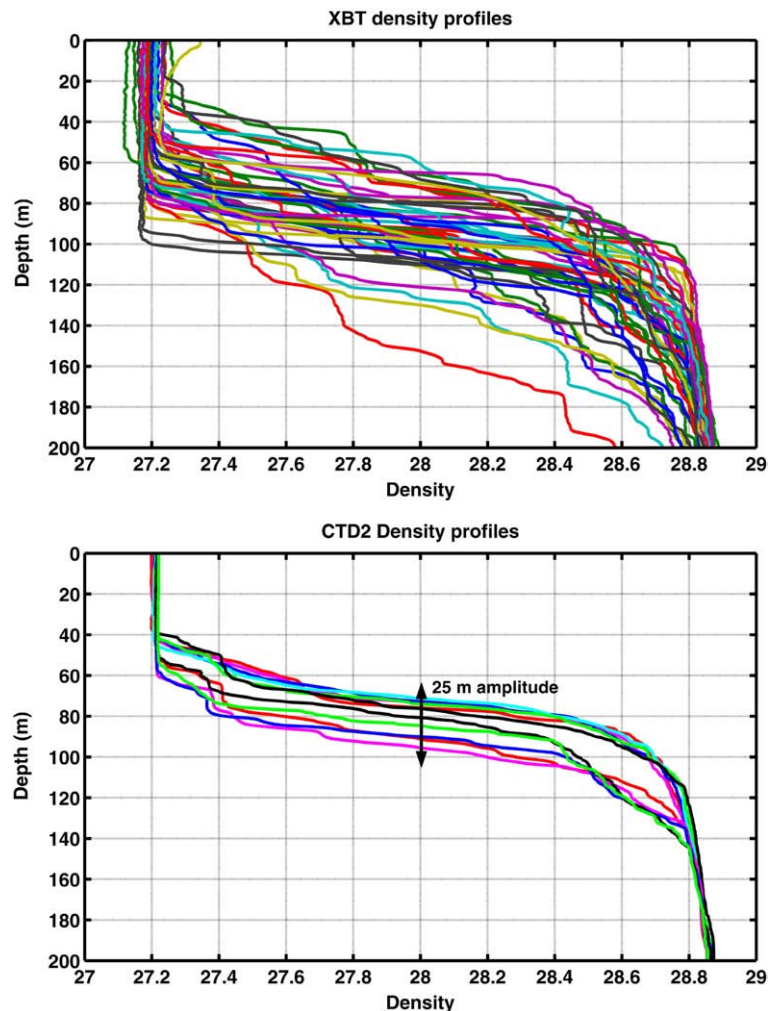

Fig. 4. Top, density profiles from all XBT probes (see Fig. 1 for locations) in the south of the strait (Ionian Sea) illustrating the variability in the water column due to the impact of internal waves. Bottom, density profiles measured by the lowered CTD probe at location (15°34′04″ E, 38°03′04″ N). The pycnocline depth has a 25 m amplitude variability illustrating the occurrence of an internal wave event. Density units are "sigma-t".

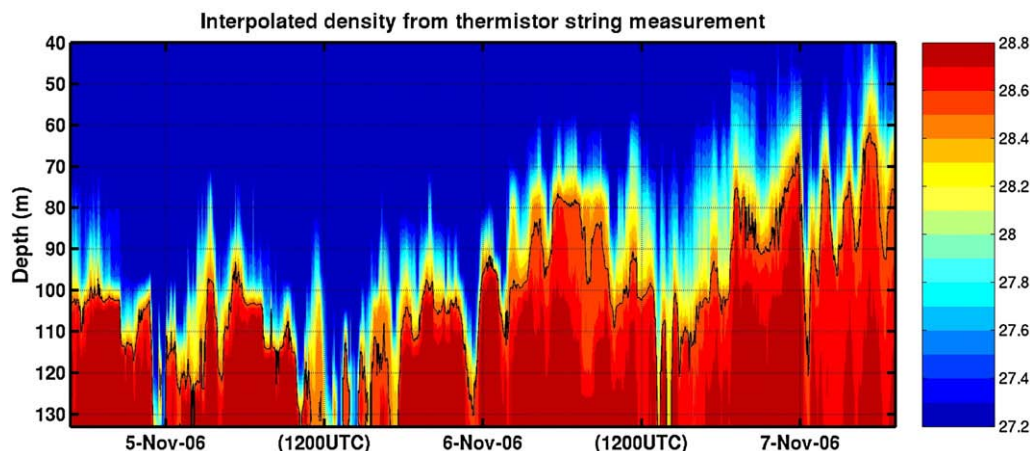## Interpolated density from thermistor string measurement

Fig. 5. Density computed from thermistor string measurements from 4 November 2006 16:48 UTC to 7 November 2006 07:12 UTC. The 28.5 density contour (corresponding to a temperature of 16 °C) is plotted to underline the temperature variability due to occurrence of internal waves. Density units are "sigma-t".

depth of the mixed layer, since one would expect more mixing and more meteorological impact closer to the coast. So, the measurements were divided in three zones (west, middle, east of the strait). An average profile was given for each zone (not shown). All this shows that the mixing is constant from the Calabrian coast (east) to the middle of the Strait and increases closer to the Sicilian coast (west). This could be due to coastal current dynamics on the eastern coast of Sicily as described in Bohm et al. (1987). The tidal mixing in Messina Strait generates a water mass that flows up to 100 km southwards along the Sicilian coast and up to 10 km offshore. This current can become unstable and lead to more mixing. On the SAR image displayed in Fig. 2, it is clearly visible that the sea surface manifestations are stronger near the Sicilian coast than further offshore or close to the Calabrian coast. The amplitude of the internal waves is larger in this shallow water region of the Sicilian coast, where the internal waves are topographically guided (Alpers et al., 1996). As the measurements were done close to the Calabrian coast and the model runs along the median of the strait, this difference is neglected in the following.

Lowered CTD probes measurements (yoyos) were done at three locations: Station 1 (15°30′19″ E, 38°03′54″ N) from 6 November 08:12 UTC to 6 November 12:50 UTC, Station 2 (15°34′04″ E, 38°03′04″ N) from 6 November 20:38 UTC to 7 November 01:47 UTC, Station 3 (15°30′19″ E, 38°03′01″ N) from 7 November 13:49 UTC to 7 November 15:07 UTC. Fig. 4 (bottom) illustrates the density profiles for the CTD measurements at station 2. The low temporal sample rate of the lowered CTD (one profile every 30 min) makes it impossible to detect the propagation of a solitary wave train as the lifting and return to equilibrium of the isopycnals is much faster, with internal solitary wave periods ranging from 8 to 30 min (Alpers and Salusti, 1983). However, the pycnocline depth varies by 25 m in 5 h of measurement clearly indicating some internal wave feature.

Finally, as done and validated in Sellschopp (1997) for high temporal resolution observation of isothermal displacements, one thermistor chain was bottom-moored about 27 km south of the sill of strait, at location (15°38′57″ E, 38°02′24″ N), from 4 November 16:48 UTC to the 7 November 07:12 UTC, with a one minute temporal resolution which allows clear observations of internal solitary wave events. The chain consisted of 10 sensors attached from 14 to 128 m depth, providing a vertical resolution of about 10 m. Fig. 5 shows the density computed from the temperature measurement of the thermistor string using the Unesco equation of state (salinity was considered constant with a value of 38.10 psu). The pycnocline depth stands around 95 m for the first day and half, and raises slowly to a 60 m depth after 6 November. Internal solitary wave train events can be identified every half day, correspond-

ing to the tidal period. Table 2 summarizes precisely the occurrence of the internal wave trains, the reversal of the tide from rema montante (northwards) to rema scendente (southwards). On average, the internal wave trains are visible 6 h after the tide reversal from North to South. Considering the hypothesis made by Alpers and Salusti (1983) that, for southwards propagating internal solitary waves, the internal bores are generated at slack waters when the flow reverses from north to south, the average speed of the internal waves train is 1.25 m s^{-1}, which is faster than the propagation speed computed from the SAR images. A difference in the stratification, in the mean current and/or the tidal cycles between the months of October and November could explain this difference. Unfortunately no SAR images were available for beginning of November. The amplitudes of the internal solitary waves range between 40 and 50 m. The trains have two to four internal solitary waves. The first and second waves are very neat in the data. This is in good agreement with the analysis of the SAR images: on Fig. 3 (middle graph), the least square fit gives a value close to four internal waves per train at 27 km south of the sill, at the thermistor string position.

This data analysis was used to tune the Lamb model (third section) to infer the right internal wave characteristics by focusing on propagation velocity, number of internal waves per train, increase in the spatial separation of the waves (as obtained from the analysis of the SAR images), and frequency and amplitude of the internal solitary waves (as observed from *in-situ* data).

Table 2
Internal wave trains (IWT) identified on the thermistor string measurement.

Internal wave trains	IWT 1	IWT 2	IWT 3	IWT 4	IW 5
Occurrence of IWT	Nov. 4th 2006 23:31 UTC	Nov. 5th 2006 11:55 UTC	Nov. 5th 2006 23:40 UTC	Nov. 6th 2006 13:15 UTC	Nov. 7th 2006 00:15 UTC
Previous tide reversal (slack waters)	Nov. 4th 2006 17:02 UTC	Nov. 5th 2006 06:05 UTC	Nov. 5th 2006 17:39 UTC	Nov. 6th 2006 06:48 UTC	Nov. 6th 2006 18:14 UTC
Δt (REV–IWT)	6:29	5:50	6:01	6:27	6:01

As the bore generated at "rema montante" on the northern side of the strait undergoes a hydraulic jump over the sill to the southern basin when the tide reverses southwards (rema scendente), the time difference between the SAR image and the tidal reversal is computed in order to get the propagation speed of the internal wave train in the south basin. The first line indicates the date and time of the IWT event, the second line indicates the time of tidal reversal from north to south (slack waters) previous to the SAR image. The last line shows the time difference between the previous tide reversal and the occurrence of the IWT.

2.3. Empirical orthogonal function analysis of thermistor chain data

An EOF analysis of the time series of density obtained from *in-situ* data and numerical simulations was carried out to gain more information on the internal wave structure.

The empirical orthogonal function (EOF) decomposition is one of a larger class of inverse techniques and is equivalent to a data reduction method (Emery and Thomson, 1997). It determines the main spatial patterns of variability as well as their variation in time and gives a measure of importance of each pattern. Each EOF mode represents a standing oscillation pattern (Preisendorfer, 1988). The projection of the data onto the EOF modes gives an estimate of how the pattern oscillates in time. These projections are called principal component time series or expansion/projection coefficients of the EOFs. Most of the variance is usually in the first few orthogonal functions and the EOFs can be employed as a filter to avoid experimental or physical noises and consider only the most important scales of variability.

In our study, the EOF analysis was applied on the vertical density anomaly obtained from the thermistor string measurements, so that the density $\sigma(z, t)$ could be written as:

$$\sigma(z,t) = \langle \sigma(z) \rangle + \sum_{n=1}^{M} \alpha_n(t)\phi_n(z) \qquad (1)$$

where $\langle \sigma(z) \rangle$ is the time-averaged vertical density profile, M is the number of considered EOFs, $\alpha_n(t)$ is the amplitude (or 'expansion coefficient') of the nth orthogonal mode at time t and $\phi_n(z)$ the nth EOF. This equation says that the time variation of the dependent scalar variable $\sigma(z,t)$ at each depth results from the linear combination of M spatial functions ϕ_n, whose amplitudes are weighted by M time-dependent coefficients $\alpha_n(t)$. The weights $\alpha_n(t)$ tell how the spatial modes ϕ_n vary with time. As there are many terminologies for EOF analysis, we insist on the fact that the use of "EOF" refers to the vertical "spatial" pattern ϕ_n and that "expansion coefficient" (or principal component, or projection coefficient) refers to the "temporal patterns" or weights $\alpha_n(t)$.

With the inherent efficiency of this statistical description, a very few empirical modes are needed to describe the fundamental variability in a very large data set and so only three modes were considered here. The first two EOFs are plotted in Fig. 6. They are very clean and smooth, representing a dynamical pattern consisting of a background stratification interacting with internal wave occurrence. Moreover, most of the variance of the measurements is in the first two EOFs (95% and 4.5%).

The amplitude of the first EOF does not change sign over the water column and has one extremum. Therefore, all the isopycnals oscillate in the same direction (Vázquez et al., 2006) with maximum displacement at 85–90 m. It represents a vertical displacement of the pycnocline. The second EOF has two extrema, as a consequence of the orthogonality constraint, and changes sign close to the first EOF maximum depth. This indicates that isopycnals are moving in opposite directions above and below the pycnocline (Vázquez et al., 2006); it can be identified as a first baroclinic mode. It represents a change in slope of the density gradient. Fig. 7 shows one density profile projected on the first EOF mode $\langle \sigma(z) \rangle + \alpha_1(t_n)\phi_1$ (left) for several random values of the time-dependent coefficient α_1 and the same density profile projected on the second EOF $\langle \sigma(z) \rangle + \alpha_2(t_n)\phi_2$ (right) for several values of time of α_2 to illustrate the previous description of the modes. As these profiles are projected on a single EOF, they are not all realistic (especially when projected on EOF2) but this illustration helps understanding the variability of the first two modes. The depth of the pycnocline increases/deepens with higher positive values of α_1 whereas the density gradient becomes steeper, even negative with higher values of α_2. Looking at Fig. 8, we see that the values of the expansion coefficients are clearly related to internal wave occurrences, both coefficients assuming much larger absolute values during internal wave events.

Interpreting EOFs must always be done cautiously as empirical modes do not correspond necessarily to true dynamical characteristics or modes of physical behaviour (Dommenget and Latif, 2002). Fortunately, by studying the data, it is clearly seen that our computed EOF do agree very well with the dynamical modes of internal waves.
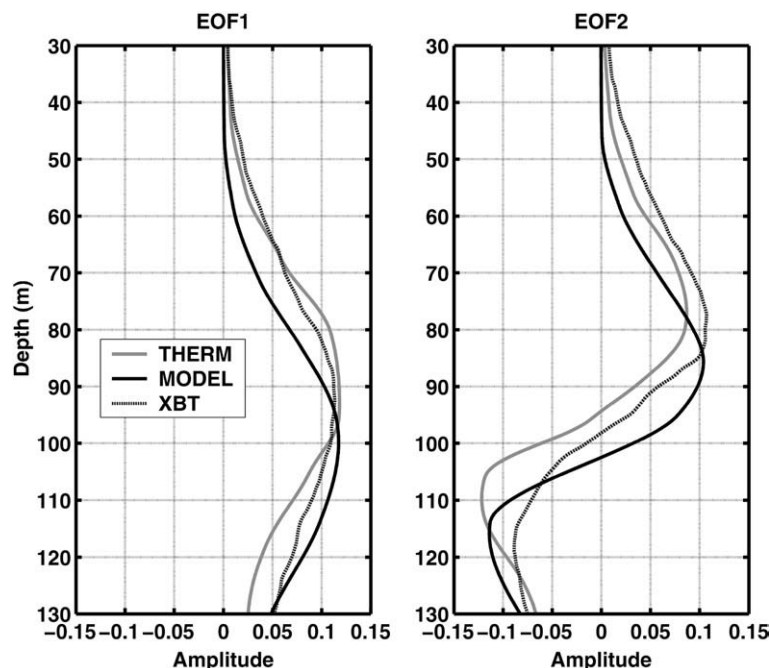

Fig. 6. Amplitude of first two EOFs ϕ_1 and ϕ_2 calculated from XBT (black dots), thermistor string (grey line) and model (black line) densities. The model fits quantitatively and qualitatively well the EOFs of the measurements. Only the first two EOF are represented as they give over 99% of the variance (95% and 4.5%).
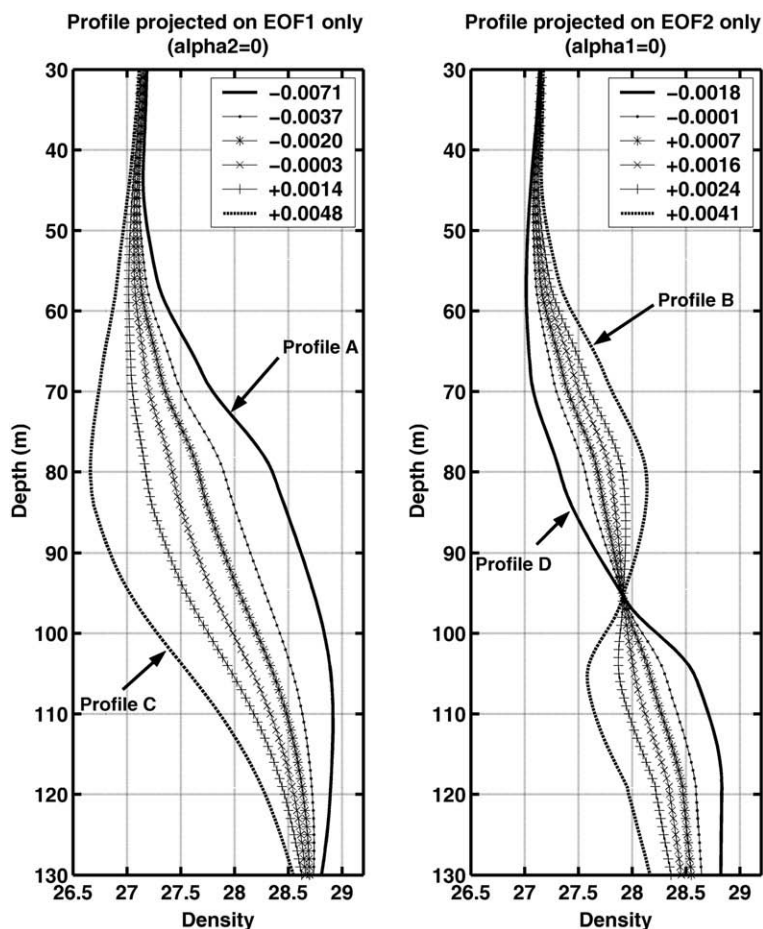
Fig. 7. On the left, one density profile is projected on EOF1 ϕ_1 ($\alpha_2(t) = 0$) for several random values of $\alpha_1(t)$. On the right, the same density profile is projected on EOF2 ϕ_2 ($\alpha_1(t) = 0$) for several random values of $\alpha_2(t)$. The values of each considered expansion coefficient are displayed in the legends. The first EOF mode shows a vertical translation of the pycnocline whereas the second EOF mode illustrates the change in slope of the density gradient.

As most of the variance was contained in the first two spatial modes and as the expansion coefficients have a similar behaviour, we looked at the scatter diagram formed by plotting the first expansion coefficient α_1 versus the second expansion coefficient α_2 in order to see if they could be related in the presence of an internal wave event. The result reveals a crescent shaped distribution (Fig. 9) meaning that the two EOF
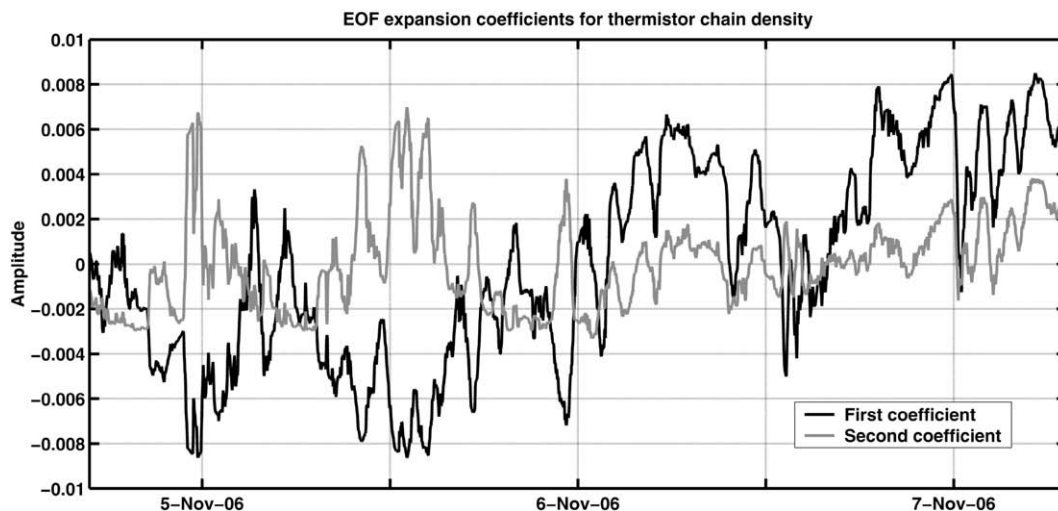

Fig. 8. Expansion coefficients for the first two EOF modes. The first expansion coefficient clearly represents the vertical oscillation of the pycnocline in time (compared with density contour 28.5 on Fig. 5). Both coefficients have stronger (absolute) values during internal wave events.
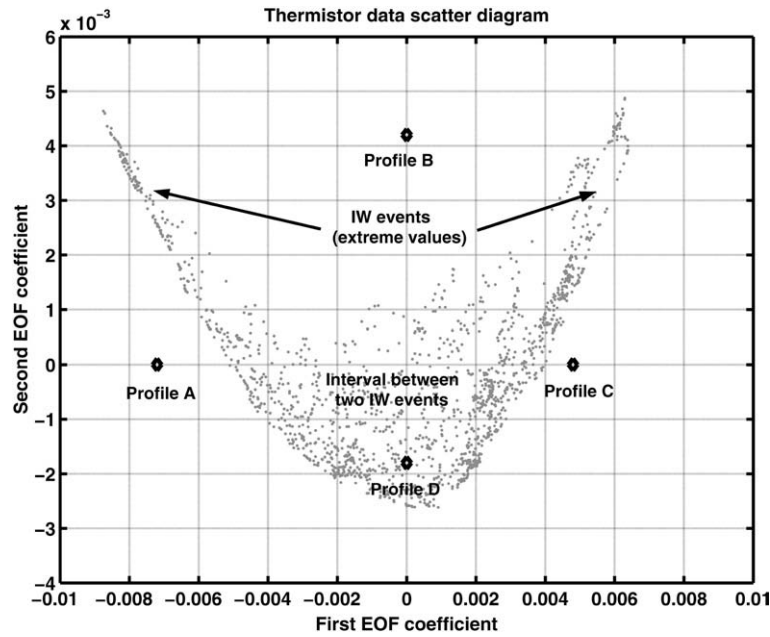
Fig. 9. Scatter diagram for the thermistor string data. The scatter diagram is obtained by plotting the first two EOF coefficients α_1 and α_2 versus one another. The "crescent shape" of the scatter diagram shows that the two main EOF expansion coefficients are not independent in the presence of internal waves. The "middle" of the cloud of points represents the interval between two internal wave events when the profile is close to its mean position. The asymptotic behavior of the cloud of points for high values of the expansion coefficients is representative of internal wave events. The black dots indicate the location of the four initial density profile coefficients for chapter 4.2. Profiles A, B and C are taken out of the cloud of points whereas profile D is taken well inside the cloud of points, at the bottom of the "crescent".

projection coefficients are not independent: $\alpha_2(t) = f(\alpha_1(t))$. The density can then be fully described as:

$$\sigma(z,t) = \langle\sigma(z)\rangle + \alpha_1(t)\phi_1(z) + \alpha_2(t)\phi_2(z), \tag{2}$$

$$= \langle\sigma(z)\rangle + \alpha_1\phi_1 + f(\alpha_1)\phi_2. \tag{3}$$

When looking at the cloud of points on Fig. 9, two regimes can be distinguished. In the centre of the distribution ($|\alpha_1| < 0.005$ and $\alpha_2 < 0$), where the cloud of points is thick and dense, α_1 takes small values meaning a weak variation of the pycnocline depth. α_2 is negative. Looking at the profiles projected on the second EOF with negative coefficients on Fig. 7, the corresponding profiles are smooth and typical of a well stratified water column. This regime represents a "rest regime" with no internal wave events. Looking now at the "branches" of the "crescent" ($|\alpha_1| > 0.005$ and $\alpha_2 > 0$), one can see how both coefficients increase in a correlated way. This regime represents typically the internal wave dynamics: when the pycnocline is depressed by the internal solitary waves (represented by the variation of α_1), the depression of the interface generates a horizontal circulation with opposite horizontal currents below and above the interface of the pycnocline thus modifying the density gradient in the pycnocline (represented by α_2). These baroclinic currents are added to the external barotropic current. Once the internal wave train has passed, this baroclinic structure disappears and we are back in the first regime.

3. Modelling

In order to confirm the crescent-shape scatter diagram obtained from the data, several numerical simulations were made using the internal wave Lamb model (Lamb, 1994).

3.1. The 2.5 dimensional internal wave Lamb model

The Lamb (1994) model is used here for simulating the generation and propagation of internal solitary waves in the Strait of Messina. It is a fully nonlinear and nonhydrostatic model. It is based on the incompressible Boussinesq equations on a rotating f-plane. In the y-direction, the velocity V is included but its derivatives with respect to the y-coordinate are neglected (hence, the designation "2.5 dimensional" representation). The x and z coordinates define a vertical plane with the x coordinate laid out along bathymetry contours in the centre of the strait. The equations of the model are:

$$V_t + V.\nabla V - fV \times \vec{k} = -\nabla P - \vec{k}\rho g, \tag{4}$$

$$\rho_t + V.\nabla\rho = 0, \tag{5}$$

$$\nabla.V = 0, \tag{6}$$

where viscosity is neglected for internal solitary wave generation and propagation (Warn Varnas et al., 2007), $V(u,v,w)$ is the velocity vector, ∇ is the three-dimensional vector gradient operator, subscript t denotes the time derivative, ρ is the density, P is the pressure, g is the gravitational acceleration, f is the Coriolis parameter taken as 9.03×10^{-5} s^{-1}, and $\vec{k}$ is the unit vector along the z-direction, z is downward. In the three-dimensional Eqs. (4)–(6) the partial derivatives with respect to y are neglected, i.e. $\partial/\partial y(.) = 0$. Thus, Eqs. (4)–(6) are equivalent to Eqs. (1a) to (1d) in Lamb (1994). Before the equations are solved, they are transformed to a terrain following coordinate system in the vertical, which leads to higher vertical resolution over the sill of the strait. The equations are solved on a domain bounded below by the topography at $z = h(z)$ and above by a free slip lid at $z = H$, H being the deep-water depth. At the upper boundary there is no normal flow and the normal derivative of the tangential velocity is set to zero. At the lower boundary rigid conditions are used, and all velocities are set to zero. The right boundary (northern basin) is treated as an outflow. On the left boundary (southern basin), the flow u_{lb} is forced by specifying the semidiurnal tidal velocity as $u_{lb} = V_T\sin(\omega t + \delta)$ where V_T is the semidiurnal tidal magnitude, ω the tidal frequency and δ the phase factor. Reflection occurs on the left and the simulation length time must be adequately chosen in order to avoid the perturbation of the physical processes by the reflected waves.

The model was initialized with 150 vertical levels, which gives a vertical resolution of 50 cm at the sill and 8 m at the southern boundary. The along-flow coordinate ranged from a 100 km south to 100 km north of the sill of the strait. Only the M2 tidal component is considered for initial tidal forcing, as this is the main tidal component in the Strait (Alpers and Salusti, 1983; Brandt et al., 1998). Several simulations were made by varying the semidiurnal tidal magnitude V_T. The topography is represented by $cosh(x,z)$ functions (Fig. 10). The density field for model initialization was derived from the thermistor chain measurements for the southern boundary and CTD surveys for the northern boundary. The model predictions are for the median of the strait. Five hypothetical moorings were implemented in the model (Fig. 10). We concentrated our analysis on "mooring 2" in the south of the strait as it corresponds to the position of the thermistor chain in the COACH06 experiment. "Mooring 2" was defined with 10 instruments ranging from 15 m depth to 132 m depth.

3.2. EOF analysis of the model outputs

As was done with the thermistor data, an EOF analysis was applied to the numerical density outputs at "mooring 2" to analyze internal waves. We stress here that we are adopting a statistical approach, not at all a deterministic approach focusing on time of release of the bore or internal wave trains precise occurrence. Variations induced by internal solitary waves are tracked by EOF modes. The numerical runs were made in order to validate the characterization of the internal waves made in paragraph 2.3.

Several runs were made by changing the initial tidal M2 component speed (respectively 0.01, 0.02, 0.03, 0.04, 0.05, 0.09 and 0.12 m s^{-1}), all initialized by the same density profile extracted from the thermistor data. Here the amplitude of the barotropic tidal component is varied to match the propagation speed of the internal solitary wave trains.

For an initial tidal speed of 0.01 m s^{-1}, the pycnocline is depressed by the initial barotropic tide but hardly any bore is generated. For an initial tidal speed of 0.09 m s^{-1}, the amplitude of the waves is unrealistic (over 200 m!) and they propagate too fast (Fig. 11).

Given the SAR figures, the run closer to the observed internal waves is the one with an initial barotropic tidal speed of 0.03 m s^{-1}.

The propagation speed of the wave train is 1.06 m s^{-1}, which is close to the propagation speed of 1.00 m s^{-1} obtained from the SAR data. At 25–30 km south of the sill, the modelled wave train evolves as 2 to 3 internal solitary waves (Fig. 11), which corresponds well to the number of waves observed at the same distance on the SAR images (Fig. 3). The amplitude of the waves (50 m) at 30 km from the sill is also close to that of the thermistor data (Fig. 5). The pycnocline displacements exhibit a pronounced signature of internal solitary wave trains. The mid pycnocline location can simulate the interface deviation for a two-layer model. Close to the sea surface there is a signature of internal solitary waves in phase with the pycnocline signature. Time evolution of pycnocline and sea surface signatures can both be compared to SAR observations. The first two EOF modes are also well illustrated. The first EOF mode is predominant when looking at the propagating internal wave train between 30 and 40 km away from the sill where all isopycnals behave similarly in the pycnocline. The second EOF mode, where isopycnals are moving in opposite directions above and below the pycnocline, is present close to the sill and up to 15 km southwards. It is important to notice that an unrealistic barotropic tidal speed (such as runs with 0.01 m s^{-1} and 0.09 m s^{-1} tidal speed) leads to wrong internal baroclinic wave features.

Looking now at the first two EOFs for the run with 0.03 m s^{-1} barotropic tidal velocity, it is seen that the EOF extrema are deeper for the model (Fig. 6) than for the data. At the southern boundary, the model is initialized by a density profile measured when the pycnocline is deeper at the beginning of the thermistor string measurement period. The thermistor string EOFs computed for the whole period of the measurement (Fig. 5) thus lead to shallower maxima because of the pycnocline rise. Nonetheless, the data EOFs and the model EOFs agree well in amplitude and shape.

4. Discussion of the simulation results and comparison with the data EOF distribution

4.1. Distribution of model expansion coefficients

To study the consistency of data expansion coefficients in a scatter diagram, the previous methodology was applied to three numerical simulations (Fig. 12) at "mooring 2": "No IW run" (initial tidal speed
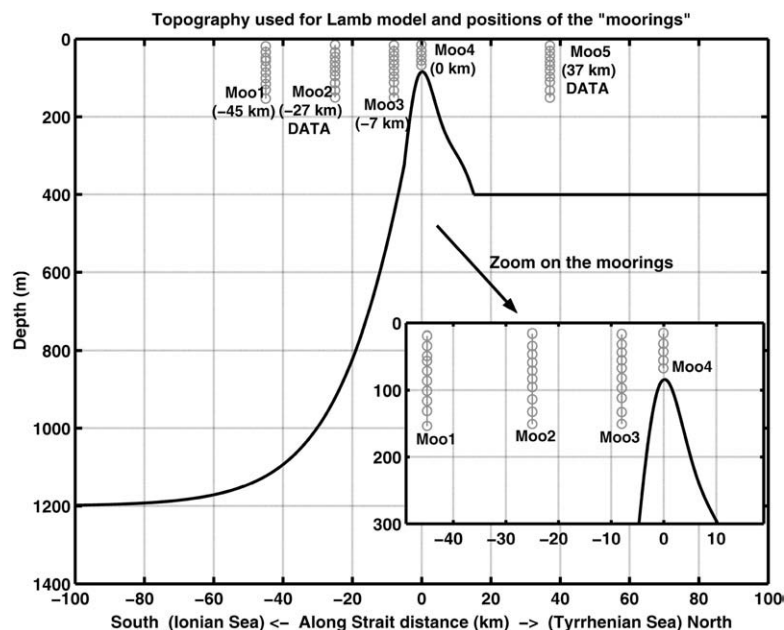

Fig. 10. Topography (black thick line) along the strait used in the 2.5D Lamb (1994) model. Five moorings, called 'Moo' on the graph (grey diamond lines), were implemented in the model. Moorings 1, 2, 3, 5 have 10 instruments on the vertical, Mooring 4 has only five instruments as it was implemented at the sill of the strait. Moorings 2 and 5 correspond to the positions of the thermistor strings deployed during the COACH06 cruise (north basin was not considered in this study).
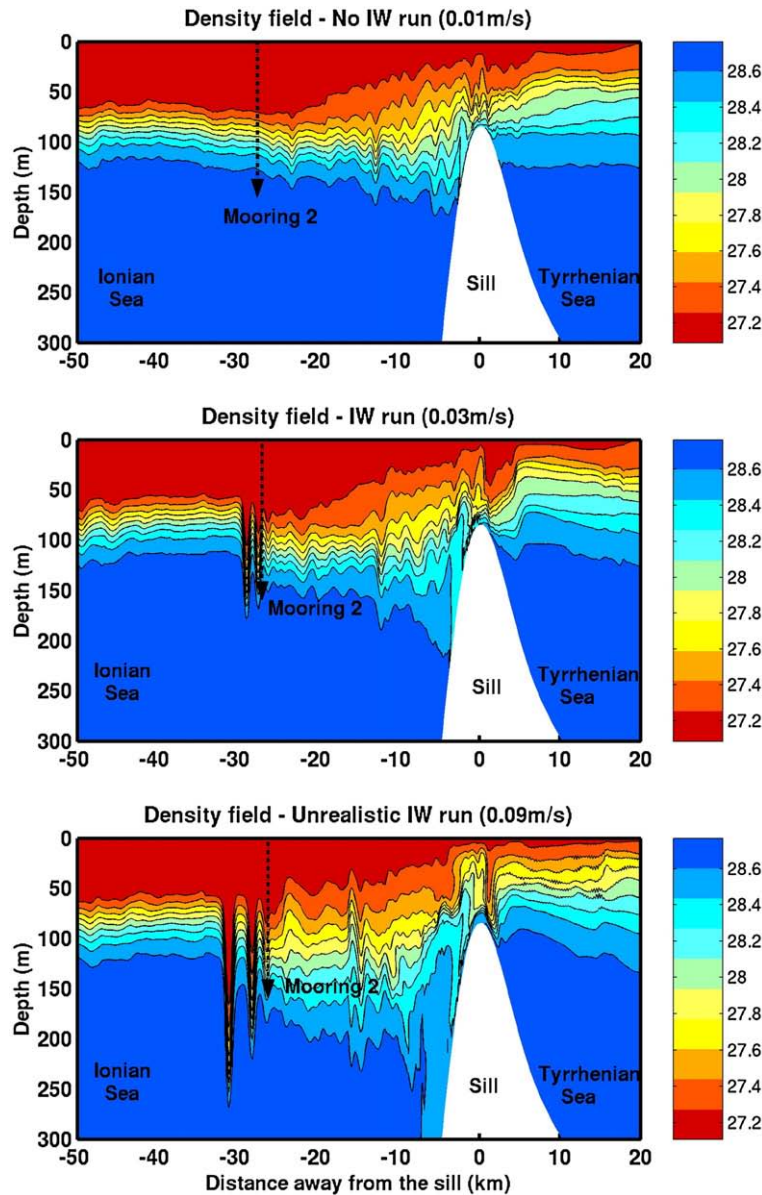
Fig. 11. 2D density fields after 20 h run for an initial M2 tidal speed of 0.01 m s^{-1} (top), 0.03 m s^{-1} (middle) and 0.09 m s^{-1} (bottom). Density units are "sigma-t". The area considered is the one illustrated in the zoom of Fig. 10. The amplitude of the internal waves is highly correlated to the initial barotropic tidal speed. If the barotropic tidal speed is too high, the internal wave features become unrealistic (bottom) for the strait of Messina. This parameter must be tuned very carefully in order to get proper internal solitary wave events.

0.01 m s^{-1}), "IW-run" (initial tidal speed 0.03 m s^{-1}) and "unrealistic IW" run (initial tidal speed 0.09 m s^{-1}) where "IW" stands for internal wave.

In the absence of internal waves (top in Fig. 12), the cloud of points is small (black dots) and centered at the cloud of points of the data (grey dots). It has a weak expansion of α_1 and very little variations of α_2. Thus the main displacement of the pycnocline is a limited vertical translation with no internal wave propagation. This is confirmed by the 2D density field on Fig. 11 (top). The depression of the pycnocline due to the bore, close to the sill, is still observed though this bore does not disintegrate into a proper internal wave train. Small vertical oscillations of the pycnocline are still generated further down the strait. These oscillations are represented by the variation of $\alpha_1(-0.0055 < \alpha_1 < 0.004)$.

As the prescribed barotropic tidal speed increases to 0.3 m s^{-1}, we observe a great expansion of the "crescent". The increase in the values of the expansion coefficients corresponds to the presence of bores and their subsequent disintegration into solitary wave trains. The middle graph in Fig. 12 shows the best fit case for a barotropic initial tidal forcing of 0.03 m s^{-1}. The model distribution in this case fits well the data cloud of points. This is confirmed by the nice internal solitary wave train observed on Fig. 11 (middle). With an initial tidal forcing of 0.09 m s^{-1}, the expansion coefficient distribution of the model does not fit that of the data anymore. The first mode interval tends towards a wider negative limit, which means the pycnocline gets too deep. The second mode has also wider positive variations where it used to be negative in the centre left of the crescent shape ($-0.002 < \alpha_1 < 0$), meaning that the pycnocline slope keeps varying while the pycnocline depth is above its mean position. This illustrates a longer time needed to return to equilibrium of the pycnocline as the internal wave characteristics are unrealistically large (propagation speed of 1.30 m s^{-1} with wave amplitude of 200 m on Fig. 11 bottom) compared with those of the data (propagation speed of 1.00 m s^{-1} with waves amplitude of 50 m).

These results confirm that incorrect physics leads to an incorrect expansion coefficient distribution, and thus that the scatter diagram is a means to identify and characterize internal solitary wave trains occurring in the area.
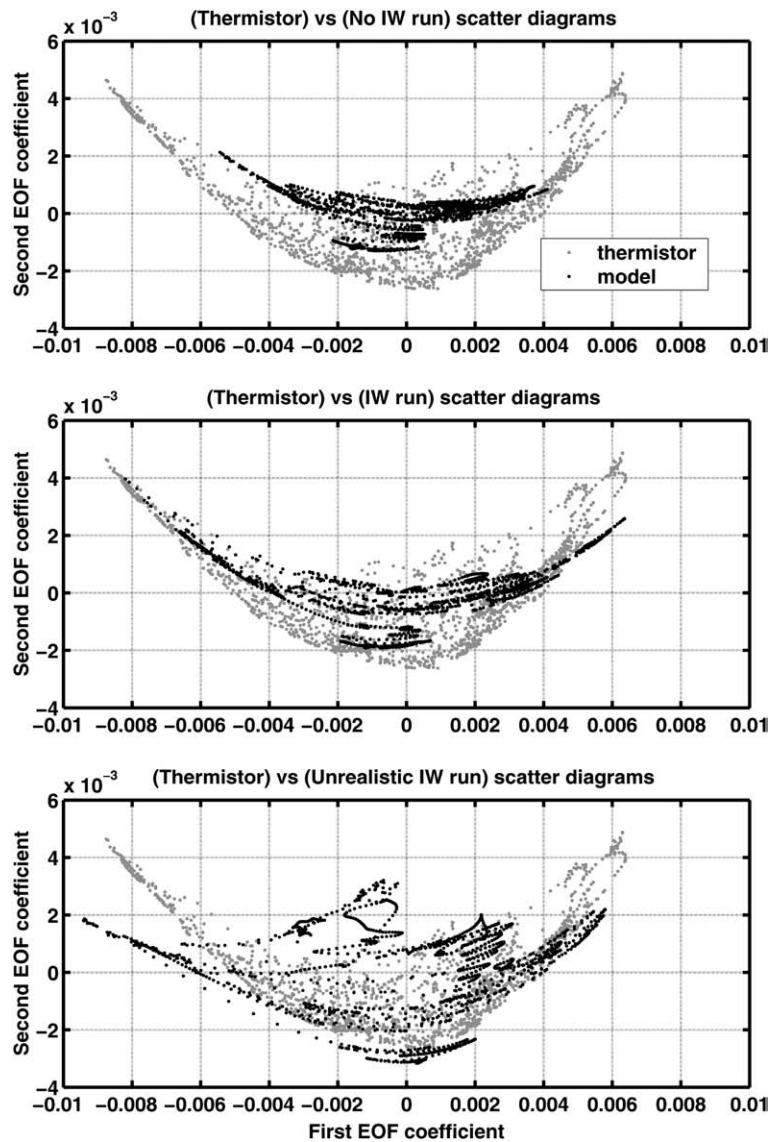
Fig. 12. Comparisons of the scatter diagrams (α_1 and α_2 versus one another) of the thermistor string and the model. The grey dots represent the scatter diagram obtained with the expansion coefficients of the density from the thermistor string. The black dots represent the scatter diagram from the model density outputs for the 'No IW' simulation (top), the 'IW' simulation (middle) and the 'Unrealistic IW' simulation (bottom), corresponding to the three simulations displayed in Fig. 11.

4.2. Model scatter diagram sensitivity to initial density profile

To study the sensitivity of the model we reconstruct initial density profiles using the EOF projection coefficients of Fig. 9, taken inside and outside the cloud of points. We then reconstruct the corresponding density profiles using Eq. (2). These profiles are called profile A ($\alpha_1 = -0.0071$, $\alpha_2 = 0$), profile B ($\alpha_1 = 0, \alpha_2 = 0.0041$), profile C ($\alpha_1 = 0.0048, \alpha_2 = 0$) and profile D ($\alpha_1 = 0, \alpha_2 = -0.0018$). They are shown in Fig. 9 by their EOF coefficients and are outlined in Fig. 7. As these profiles are not reconstructed by the full combination of all EOF modes, they are not necessarily realistic, as the strong density inversion in profile B shows, but this will give hints on the model behaviour and stability.

Profiles A and C are reconstructed with an anomaly perturbation that represents an up and down movement of the pycnocline (Fig. 7 left). On profile A, the pycnocline (inflexion point) is higher (70 m) than the mean pycnocline depth (95 m). On the contrary, profile C, with a high positive α_1 coefficient has a pycnocline depth deeper than the mean profile. For these two profiles, α_2 is null, meaning that we have filtered out the second mode.

For profiles B and D, α_1 is null. The profiles are reconstructed using only the second EOF, meaning that the pycnocline depth corresponds

to the mean value observed in the data and that the pycnocline vertical translation is filtered out (no EOF1). For profile B, an unstable slope perturbation of the pycnocline is introduced: α_2 has a very high positive value, characteristic of a strong steepening of the slope of the density gradient leading to density inversion (Fig. 7). EOF2 represents only 4.5% of the variability as mentioned in Section 3.2. Reconstructing the profiles by filtering the first or second EOF, specially the first EOF (95% of the variability), may not lead to stable profiles, which is the case for this latter case.

Profiles A, B and C are taken out of the cloud of points (Fig. 9). The EOF coefficients of profile D have been chosen in order to locate the density profile in the bottom and middle of the cloud of points. The reconstructed profile is characteristic of a stable stratified water column with a mean pycnocline depth at 95 m and a strong gradient (small pycnocline thickness). The aim is to study the reaction of the model to initialisation from density profiles that are different from the measurements. The scatter diagrams for each profile are plotted in Fig. 13.

Our first remark is that wherever the initial profile has been chosen inside or outside the data distribution of points, the expansion of the model scatter diagram fits into that of the data.
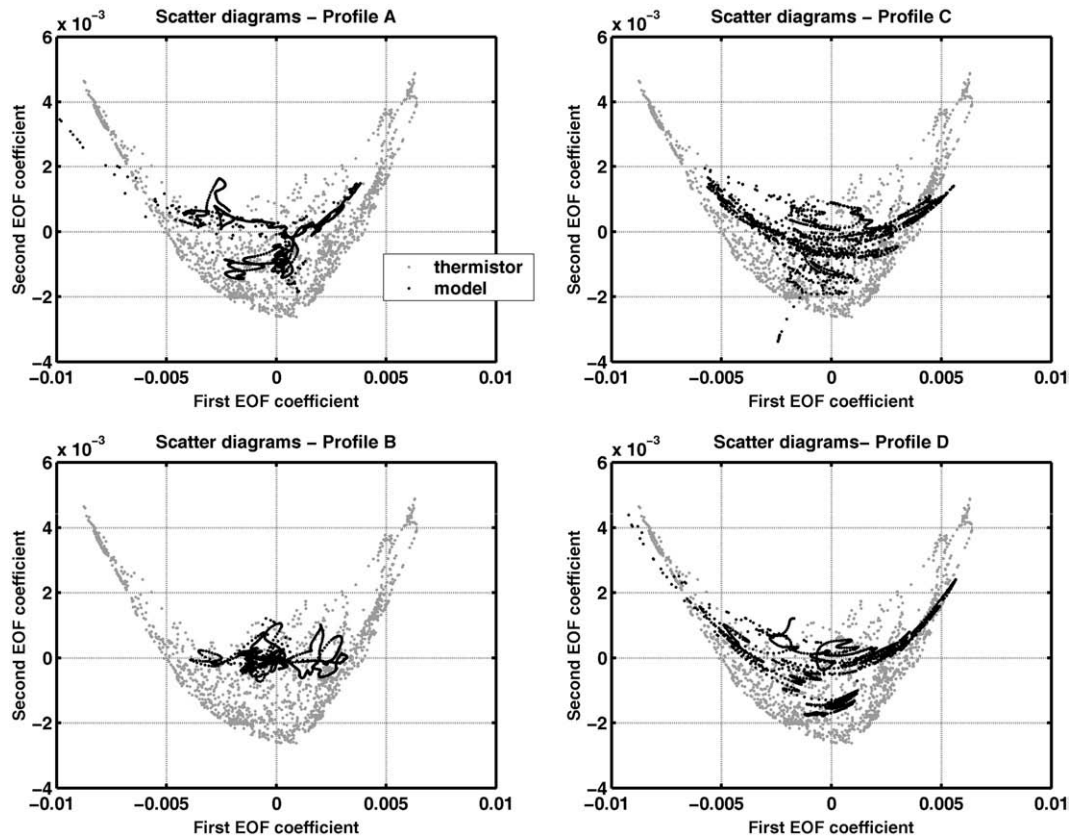
Fig. 13. Comparisons of data/model scatter diagrams. The grey dots represent the scatter diagram from the thermistor string data. The black dots represent the scatter diagram from the model outputs for a run initialized by density profile A (top left), by density profile C (top right), by density profile B (bottom right) and by density profile D (the four profiles are highlighted on Fig. 9). A, B and C are outside the cloud of points. The best data/model fit is for the run initialized by profile D which is close to the bottom of the "crescent".

Profile B is representative of a density profile with a very strong shear leading to a density inversion. The corresponding cloud of points looks random with no specific shape (Fig. 13 bottom left). The distribution is centred around the origin with excursions of α_1 that reflect small depth variations: the density inversion leads to instability and creates small oscillations of the pycnocline interface ($-0.004 < \alpha_1 < 0.003$) with a very weak shear ($-0.001 < \alpha_2 < 0.001$). No crescent type of curvature is present in this case showing that the modeled density evolves around the mean density profile. The initial density inversion is smoothed by model dynamics. The 4.5% perturbation input through EOF2 does not lead to a random behaviour of the model. The model is very stable and sticks to the average profile. The weak shear means an absence of internal solitary wave events.

Initializing the model with a profile whose pycnocline is less deep, profile A, results in the scatter diagram shown in Fig. 13 top left. The variation consists of line movements with changing shapes and direction. A light crescent shape starts appearing. There is still some random behavior around the mean position. For profiles C and D, the distribution of the coefficients contains crescent type curvatures (Fig. 13 right, top and bottom), similar to the variations of the tuned model distributions in Fig. 12. The gradient around the inflexion point of profile D is stronger than the gradient of profile C (Fig. 7), meaning that the pycnocline is thicker for profile C (about 100 m) than for profile D (about 70 m). It is observed on the scatter diagram of profile C that α_1 is not reaching the extreme values of the data coefficient value interval although the initial downward displacement of the pycnocline for profile C results in a scatter diagram that is in range of observed scatter diagram. There is an internal wave train, but as the pycnocline is thicker, the amplitude of the vertical displacement is not as strong as for profile D (5 to 10 m difference, not shown). Another consequence of the gradient difference is that, the slope being smoother for profile C, the horizontal circulation generated by the

interface slope will be weaker and thus the shear will not be as strong: the internal solitary waves have a steeper front for profile D. The smoother pycnocline gradient of profile C leads to "weaker" internal waves (smaller amplitude) than the observed ones. Profile D is the profile that generates the internal wave train closer to the observed characteristics. It is also the one whose distribution fits best the data scatter diagram.

All four of the constructed initial profiles, Fig. 9, lead to scatter diagrams that are in range of observations (Fig. 13). This suggests that variations of initial pycnocline depth and slope of pycnocline are tolerable in model initialization. The agreement of the model predicted scatter diagrams with the observations shows that the Lamb (1994) model represents well the physics and phenomena taking place.

5. Summary and conclusions

The Strait of Messina with its shallow sill and strong tidal currents leading to strong interfacial depressions is an important place of internal bore generation and internal solitary wave occurrence. The nonlinear, non-hydrostatic Lamb model, initialized by two density profiles on each side of the strait, behaves very well while reproducing internal wave characteristics and is in a very good qualitative and quantitative agreement with SAR and in-situ data. The agreement of model with measurements indicates that the Lamb (1994) model represents well the physics and variability of the internal wave dynamics and phenomena taking place.

In this study, we have presented an original method for internal wave detection in the south of the Strait of Messina. This characterization is based on EOF analysis. It consists in studying the scatter diagram formed by the expansion coefficient of the first EOF mode versus the expansion coefficient of the second EOF mode. When there

is no internal wave, the scatter diagram is small and the projection on the first mode is less important than the one on the second mode. When there is an internal wave event, the intervals of the expansion coefficients become wider so that the scatter diagram assumes a crescent shape. The EOF expansion coefficients and their scatter diagram reflect the presence of internal bores and internal waves. As the scatter diagram has a well defined crescent shape distribution, a polynomial can be fitted to the cloud of points and thus give a relation between the two expansion coefficients. The validity of this methodology was tested by comparing model outputs with *in-situ* data. The model was initialized with a density profile derived from thermistor chain and CTD probe measurements. The tuning was accomplished by varying the tidal forcing. The predicted internal wave speed and amplitude were matched with SAR and *in-situ* observations. The scatter diagram of the model output and the scatter diagram derived from measurements are in good agreement. It means that the model can predict well the amplitude of the two main EOF modes, but also the difference in phase between these modes.

This methodology could be interesting for operational oceanography or tactical applications in navy needs. If the scatter diagram is well shaped as observed in the Strait of Messina, a polynomial function can be fitted to the crescent shape and could be derived for various regions of interest. This polynomial represents the relation between the first two expansion coefficients. It could be sampled in order to reconstruct density or sound speed vertical profiles using the first two EOF vertical modes. The fitted function is then a way to represent all the water column profiles/physics that can be encountered in the area. Once this function is established, there is no more need for *in-situ* measurements or highly demanding computational cost modelling. Navy forces could then simulate any acoustical scenario they wish to study for any chosen profile, or may combine the curve fitted to the scatter diagram with systematic application of acoustical propagation models and thus get a complete acoustical variability map of the area.

Acknowledgments

References

Alpers, W., Salusti, E., 1983. Scylla and Charybdis observed from space. Journal of Geophysical Research 88 (C3), 1800–1808.

Alpers, W., Brandt, P., Rubino, A., Backhaus, J.O., 1996: Recent contributions of remote sensing to the study of internal waves in the straits of Gibraltar and Messina. Dynamics of Mediterranean straits and channels. CIESM Science Series n°2, Bulletin de l'Institut Océanographique 17, Monaco, 21–40.

Apel, J., Jackson, C., 2004. Synthetic Aperture Radar Marine User's Manual. United States Department of Commerce, National Oceanic and Atmospheric Administration, Washington. 464 pp.

Baines, P., 1973. The generation of internal tides by flat-bump topography. Deep Sea Research 20, 179–205.

Baines, P., 1982. On internal tide generation models. Deep Sea Research 29, 307–338.

Bignami, F., Salusti, E., 1990. Tidal currents and transient phenomena in the Strait of Messina: a review. The Physical Oceanography of Sea Straits 95–124.

Bohm, E., Magazzu, G., Wald, L., Zoccolotti, M.-L., 1987. Coastal currents on the Sicilian shelf south of Messina. Oceanologica Acta 10 (2), 137–142.

Brandt, P., Rubino, A., Alpers, W., Backhaus, J.O., 1997. Internal waves in the Strait of Messina studied by a numerical model and synthetic aperture radar images from ERS satellites. Journal Physical Oceanography 27 (5), 648–663.

Brandt, P., Rubino, A., Quadfasel, D., Alpers, W., Sellschopp, J., Fiekas, H.-V., 1998. Evidence for the influence of Atlantic–Ionian stream fluctuations on the tidally induced internal dynamics in the Strait of Messina. Journal of Physical Oceanography 29 (5), 1071–1080.

Defant, A., 1940. Scilla e Carridi e le correnti di marea nello Stretto di Messina. Geophisica Pura e Applicata 2, 93–112.

Defant, A., 1961. Tides in the Mediterranean and adjacent seas. Observations and Discussion. Physical Oceanography, vol. 1. Pergamon Press, pp. 364–456. Chapter 12.

Del Ricco, R., 1982. Numerical model of the internal calculation of a strait under the influence of the tides, and its application to the Messina Strait. Il Nuovo Cimento 5 (C1), 21–45.

Dommenget, D., Latif, M., 2002. A cautionary note on the interpretation of EOF. Journal of Climate 15 (2), 216–225.

Emery, W., Thomson, R., 1997. Data Analysis Methods in Physical Oceanography. Elsevier, Amsterdam, Netherlands. 634 pp.

Gerkema, T., 1994: Nonlinear dispersive internal tides: generation models for a rotating ocean, Ph.D. Thesis of Utrecht University, 150 pp.

Global Ocean Associates (GOA), 2004. Strait of Messina. An Atlas of Oceanic Solitary Waves, 199–206. Study Prepared for the Office of Naval Research – Code 322 PO. WWW page. http://www.internalwaveatlas.com/.

Griffa, A., Marullo, S., Santoleri, R., Viola, A., 1986. Internal nonlinear tidal waves generated in the Strait of Messina. Continental Shelf Research 6 (5), 677–687.

Hopkins, T.S., Salusti, E., Settimi, D., 1984. Tidal forcing of the water mass interface in the Strait of Messina. Journal of Geophysical Research 89 (C2), 2013–2024.

Lamb, K., 1994. Numerical experiments of internal wave generation by strong tidal flow across a finite amplitude bank edge. Journal of Geophysical Research 99 (C1), 843–864.

Marullo, S., Santoleri, R., 1986. Fronts and internal currents at the northern mouth of the Strait of Messina. Il Nuovo Cimento 9C (3), 701–713.

Mosetti, F., 1988. Some news on the currents in the Strait of Messina. Bolletino di Oceanologia Teorica e Applicata VI (3), 119–201.

Osborne, A.R., Burch, T.L., 1980. Internal solitons in the Andaman Sea. Science 280, 451–460.

Preisendorfer, R.W., 1988. Principal Component Analysis in Meteorology and Oceanography. Elsevier. 425 pp.

Sapia, A., Salusti, E., 1987. Observation on nonlinear internal solitary wave trains at the northern and southern mouths of the Strait of Messina. Deep Sea Research 34, 1081–1092.

Sellschopp, J., 1997. A towed CTD chain for high resolution hydrography. Deep Sea Research 44, 147–165.

Vázquez, A., Stashchuk, N., Vlasenko, V., Bruno, M., Izquierdo, A., Gallacher, P.C., 2006. Evidence of multimodal structure of the baroclinic tide in the Strait of Gibraltar. Geophysical Research Letters (33) 6 pp.

Vercelli, F., 1925. Il regime delle correnti e delle mare nello Stretto di Messina. Commissione Internazionale del Mediterraneo. Campagne della R. Nave Marsigli negli anni 1922 e 1923. 209 pp.

Warn Varnas, A., Chin-Bing, S.A., King, D.B., Hallock, Z., Hawkins, J.A., 2003. Ocean-acoustic solitary wave studies and predictions. Surveys in Geophysics 24, 39–79.

Warn Varnas, A., Hawkins, J.A., Lamb, K.G., Texeira, M., 2005. Yellow Sea ocean-acoustic solitary wave modelling studies. Journal of Geophysical Research 110 (C08).

Warn Varnas, A., Hawkins, J., Smolarkiewicz, P.K., Chin-Bing, S.A., King, D., Hallock, Z., 2007. Solitary waves effects north of Strait of Messina. Ocean Modelling 18, 97–121.

Zeilon, N., 1912. On the tidal boundary waves and related hydrodynamical problems. Kungl. Svenska Vetenskapsakademiens Handlingar 47 (4) 46 pp.